# Geophysical Research Letters

**Key Points:**
- Previously undescribed delayed island mass effects can generate intense blooms decoupled from island fertilization both in time and in space
- These occur when diazotrophs slowly utilize excess phosphate and iron after a classical island effect while being advected away from islands
- The fertilizing impact of islands on phytoplankton may thus currently be largely underestimated in the oligotrophic ocean

**Supporting Information:**
- Supporting Information S1
- Movie S1

**Correspondence to:**
M. Messié,
monique@mbari.org

## The Delayed Island Mass Effect: How Islands can Remotely Trigger Blooms in the Oligotrophic Ocean

**Monique Messié[1,2], Anne Petrenko[1], Andrea M. Doglioli[1], Clément Aldebert[1], Elodie Martinez[3], Guillaume Koenig[1], Sophie Bonnet[1], and Thierry Moutin[1]**

[1]Aix Marseille Univ., Université de Toulon, CNRS, IRD, MIO UM 110, Marseille, France, [2]Monterey Bay Aquarium Research Institute, Moss Landing, CA, USA, [3]University of Brest, Ifremer, CNRS, IRD, Laboratoire d'Océanographie Physique et Spatiale (LOPS), IUEM, Brest, France

**Abstract** In oligotrophic gyres of the tropical ocean, islands can enhance phytoplankton biomass and create hotspots of productivity and biodiversity. This "island mass effect" (IME) is typically identified by increased chlorophyll concentrations next to an island. Here we use a simple plankton model in a Lagrangian framework to represent an unexplained open ocean bloom, demonstrating how islands could have triggered it remotely. This new type of IME, termed "delayed IME," occurs when nitrate is limiting, N:P ratios are low, and excess phosphate and iron remain in water masses after an initial bloom associated with a "classical" IME. Nitrogen fixers then slowly utilize leftover phosphate and iron while water masses get advected away, resulting in a bloom decoupled in time (several weeks) and space (hundreds of kilometers) from island-driven nutrient supply. This study suggests that the fertilizing effect of islands on phytoplankton may have been largely underestimated.

**Plain Language Summary** In the poor and nutrient-depleted waters of the tropical Pacific, islands act as sources of nutrients fertilizing nearby waters. These nutrients are consumed by microscopic photosynthesizing algae, the phytoplankton. The resulting phytoplankton enrichments (blooms) in turn support productive ecosystems. This phenomenon, termed the "island mass effect," has been known for 60 years and is classically defined by increased chlorophyll (representing phytoplankton biomass) next to an island. Blooms also occur in the open ocean and are usually attributed to vertical processes such as mixing or uplifting that locally supply nutrients from subsurface reservoirs. In this paper, we demonstrate that a different type of island mass effect exists, where the phytoplankton response is delayed because they grow very slowly. These blooms are supported by the nitrogen fixer *Trichodesmium*. Since phytoplankton get carried away from islands by oceanic currents while they grow, this can lead to a bloom located hundreds of kilometers away with no apparent connection to the islands. Nutrient inputs by islands followed by advection can thus trigger remote blooms in the open ocean. Our study suggests that the fertilizing effect of islands may currently be largely underestimated, particularly in the warm waters of the tropical Pacific where *Trichodesmimum* is common.

## 1. Introduction

In the mostly oligotrophic tropical ocean, phytoplankton blooms sometimes do occur, dramatically increasing local production (Behrenfeld & Boss, 2014; Messié et al., 2006; Ryan et al., 2002; Wilson et al., 2008; Wilson & Qiu, 2008). These blooms are triggered by an unusual supply of nutrients often resulting from short-lived vertical transport (Johnson et al., 2010; Wilson & Qiu, 2008) driven by (sub)mesoscale oceanic circulation (Mahadevan , 2016; Ryan et al., 2002), winds (Menkes et al., 2016), or a combination of both (McGillicuddy et al., 2007). Additional processes initiating and enhancing blooms include vertically migrating phytoplankton (Wilson et al., 2008), dispersion/dilution (Lehahn et al., 2017), seasonal mixing followed by stratification (Dore et al., 2008; Moutin et al., 2018), and island-driven nutrient supply (Gove et al., 2016; Wilson & Qiu, 2008).

The fertilizing effect of islands on oceanic productivity has been known for decades. Termed the island mass effect (IME) by Doty and Oguri (1956), this process is almost ubiquitous across the tropical Pacific (Gove et al., 2016). In its classical sense, the IME is characterized by an inverse relationship between distance to
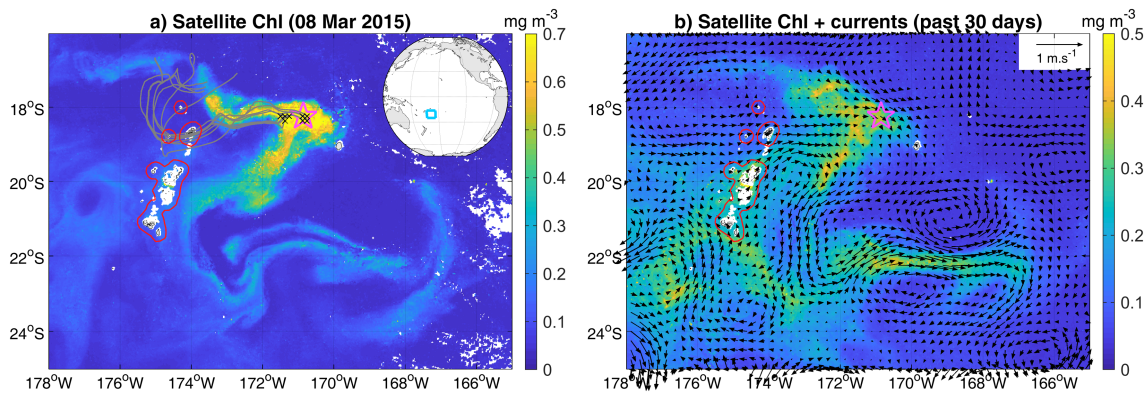
**Figure 1.** Satellite-derived contextual information. The Tonga Islands are visible near 175°W; the region within 15 km of Tonga major coastlines is contoured in red. The pink star represents station Long Duration B (LD-B) occupied during 15–20 March 2015. (a) Chl observed at the peak of the LD-B bloom. Reproducing previous results (de Verneil et al., 2017; Rousselet et al., 2018), gray lines display 60-day backward Lagrangian trajectories initialized at high-Chl patches near LD-B (Chl > 0.75 mg m$^{-3}$, black crosses). (b) Chl and surface currents observed during the previous 30 days, providing information on water mass pathway and bloom generation (note the different color bar).

an island and phytoplankton biomass and/or productivity, often represented by surface chlorophyll concentration (Chl). Biological enrichments are not always confined near the islands; Chl can peak downstream when lee eddies form (Hasegawa et al., 2009; Messié et al., 2006), and Chl enrichments can be spread by currents over hundreds of kilometers (Shiozaki et al., 2014; Signorini et al., 1999). However, including in these cases, IMEs described in the literature (hereafter "classical IMEs") always remain characterized by increased Chl spatially connected to an island.

In this context, a spectacular bloom observed from space in the western tropical South Pacific early 2015 is puzzling (Figure 1). The bloom occurred during the Oligotrophy to UlTra-oligotrophy PACific Experiment (OUTPACE) oceanographic cruise (Moutin et al., 2017) and was targeted by a Long Duration station (LD-B) due to its unusually high Chl for the region (>0.9 mg m$^{-3}$). In order to study fine-scale physical-biological coupling, high-resolution measurements were performed when the vessel reached the bloom a week after its satellite-detected peak. Surprisingly, physical data revealed a stratified water column with no evidence of mixing, upwelling, or submesoscale activity (de Verneil et al., 2017). At the same time, shipboard $^{15}N_2$ isotopic measurements unveiled very high nitrogen fixation rates sustaining nearly all new primary production (Caffin, Moutin, et al., 2018), mostly supported by the diazotroph *Trichodesmium* (Bonnet et al., 2018). While nitrogen fixation is common in the region (Bonnet et al., 2017, 2018; Shiozaki et al., 2014), the process responsible for supplying enough nutrients to support this remarkably high biological production is unclear. High phosphate waters had been advected from the eastern gyre (Bonnet et al., 2017), but the origin of iron remained a mystery, especially since diazotrophs need considerably more iron than nondiazotrophic phytoplankton (Berman-Frank et al., 2001). Local stratification ruled out vertical transport or mixing, and atmospheric deposition was low (Guieu et al., 2018). The only plausible hypothesis was offered by de Verneil et al. (2017), who suggested that iron was provided by an island contact. Indeed, although traveling on average westward, the eastern gyre waters passed near the Tonga Islands early February before they recirculated eastward toward LD-B (Figure 1, gray).

In contrast to previous reports of island-driven *Trichodesmium* blooms (Shiozaki et al., 2014), however, the LD-B bloom is clearly disconnected from the Tonga Islands (Figure 1). The classical IME definition thus does not apply and whether the bloom was triggered by islands remains to be demonstrated. We propose that the LD-B bloom is an undescribed type of IME, termed "delayed IME," where the phytoplankton respond so slowly to island fertilization that the bloom becomes separated from the islands as water masses are advected away. This hypothesis was tested first by investigating a potential nutrient release by the Tonga Islands and then by modeling the LD-B bloom using exclusively an island nutrient source and surface advection. Our simulations demonstrate how the Tonga Islands could have indeed triggered the bloom and provide a proof of concept for the existence of the delayed IME.

## 2. Materials and Methods

### 2.1. Data Sets and Lagrangian Analysis

Satellite-derived surface Chl and currents were produced specifically for OUTPACE by Ssalto/Duacs and CLS with support from TOSCA/CNES. A complete description and validation can be found in de Verneil et al. (2017) and Rousselet et al. (2018). Briefly, surface Chl (available from 2 December 2014 to 10 May 2015, 1/50° daily) were obtained from Suomi/National Polar-Orbiting Partnership/Visible Infrared Imaging Radiometer Suite (VIIRS) measurements and computed as 5-day weighted averages; resulting concentrations agree well with in situ underway Chl (Rousselet et al., 2018). Surface currents (1/8° daily) combine absolute geostrophic velocities, wind-induced Ekman circulation relative to 15 m, and a cyclogeostrophy correction. These custom products provide higher spatial and temporal resolution, and better quality, than the typically available global products. Following Gove et al. (2016), shallow pixels were removed as they were potentially contaminated by bottom reflectance (white pixels near Tonga in Figure 1: minimum depth < 30 m according to ETOPO1 bathymetry, extended by one additional pixel in all directions). Precipitation was obtained from the Global Precipitation Measurement (GPM) project (Integrated Multi-Satellite Retrievals IMERG v06, 0.1° daily; Huffman et al., 2019).

Ninety-day forward and backward Lagrangian trajectories, initialized at the center of each of the 83 current pixels located within 15 km of the major Tonga coastlines (15-km Tonga region; red contour in Figure 1) were computed for each of the 160 days of the Chl time period. The Lagrangian diagnostic tool Ariane was used (Blanke & Raynaud, 1997), with a time step of 0.1 day. East/west water mass origin was defined for each pixel as the mean longitude during the previous 90 days minus the pixel longitude, as eastern waters are likely phosphate rich (Bonnet et al., 2017; Moutin et al., 2008). Along-trajectory Chl was obtained by spatially interpolating smoothed Chl maps from the nearest day, generated to minimize data noise and gaps due to clouds using two iterations of spatial median filtering followed by a temporal linear interpolation of gaps not exceeding 5 days. For each trajectory, the average Chl 5- to 10-day upstream was termed Chl_upstream, and the Chl increase when passing by the islands was defined as ΔChl = Chl(0) − Chl_upstream (see supporting information Figure S1).

### 2.2. The Growth-Advection Approach

A simple plankton model was used, representing three nutrients (nitrogen N, phosphate P, and iron Fe), two phytoplankton (nondiazotrophic phytoplankton *Phy* and *Trichodesmium Tri*), and one zooplankton (*Z*; Text S1, Figure S2). Beyond its $N_2$-fixing capability, *Tri* differs from *Phy* by its much slower maximum growth rate ($0.27\,\mathrm{day}^{-1}$ vs. $1\,\mathrm{day}^{-1}$) and its closure term (grazing for *Phy* vs. death for *Tri*; see details in Text S1). *Tri* death includes a programmed cell death (PCD), likely responsible for the LD-B bloom demise (Spungin et al., 2018), by which *Trichodesmium* blooms can collapse in a few days in response to nutrient stress (Berman-Frank et al., 2004). Modeled Chl follows assumed C:Chl ratios for *Phy* and *Tri*. The full model description, equations, and parameters are given in Text S1 and Table S1.

The plankton model was coupled to island-driven nutrient supply and oceanic advection using a "growth-advection" method developed off California (Messié & Chavez, 2017). The method considers the evolution of plankton communities within the surface mixed layer of a water mass, as triggered by a fertilization process (here the IME) and advected by surface currents. Concretely, plankton biomass is simulated over time following an initial input of nutrients and mapped on Lagrangian trajectories. Initial conditions constrain the intensity and timing of the Chl peaks, and surface currents dictate their location.

Daily simulations were initialized within the 15-km Tonga region at the same locations as Lagrangian trajectories, with initial plankton concentrations constrained by Chl_upstream (Text S1). Initial nutrient concentrations N(0), P(0), and Fe(0) represent island-driven nutrient supply plus upstream concentrations (only for P). Because N-limited *Phy* grows faster and drives the initial bloom, N(0) was set proportional to ΔChl. P(0) was proportional to N(0) in Redfield proportions, with an additional P source when water masses originated from the east. Finally, the Tonga Islands being volcanic, the island bedrock and/or sediments are likely iron rich and can represent a significant source of iron (Blain et al., 2008; Palacios, 2002; Raapoto et al., 2019). Submarine groundwater discharge may also release iron, particularly for small tropical islands like Tonga (Moosdorf et al., 2015). Past studies found links between IMEs and surface currents with no evidence of upwelling and proposed that turbulent mixing entrains iron-rich waters (Martinez &

Maamaatuaiahutapu, 2004; Signorini et al., 1999). Fe(0) was thus proportional to current speed. All initialization parameters are given in Table S2.

Daily runs were computed from 2 December 2014 to 15 April 2015 by mapping 90-day plankton model output initialized daily onto the corresponding forward Lagrangian trajectory. Horizontal and vertical mixing was neglected (see Messié & Chavez, 2017 for more details on the method). The daily runs were then combined into 1/8° daily gridded maps by keeping, for each day and each pixel, the maximum value from all runs. The maximum rather than the mean was used to avoid unrealistic dilution by low-Chl trajectories. A 5-day weighted average was then computed, following the method applied to satellite Chl.

### 2.3. Model Optimization

The model solution depends on a number of constants used to parameterize the plankton model and its initialization (Tables S1 and S2). Most of the plankton model parameters were obtained from the literature and/or from OUTPACE measurements. Some parameters were unknown either because of a process never having been modeled before, namely, the PCD, or because no data were available to constrain them, such as parameters controlling initialization in the island vicinity (which was not sampled during OUTPACE). These parameters were first manually roughly tuned so that the model approximately represented satellite Chl. The corresponding model solution reproduced the major Chl blooms, although their timing was off by a few days (Figure S3). Then the parameters were fine-tuned using a gradient-based optimization method in order to best fit observations of satellite Chl (Text S2). The method optimized a cost function based on RMS differences of modeled and satellite Chl in delayed IME regions; classical IMEs were thus not optimized and were overestimated (Figure S3). Details on the cost function, the optimization method, and its results are provided in Text S2 and Figure S3.

## 3. Results and Discussion

### 3.1. Island-Driven Nutrient Supply

A significant satellite Chl increase when passing by the islands (ΔChl) reveals an island-driven supply of nutrients supporting a classical IME. Two high-ΔChl events were observed during the period of study (Figure 2a, blue shading), indicating that the Tonga Islands can effectively act as a nutrient source. At the peak of both events (11 January and 9 February 2015), ΔChl represented a >90% increase relative to upstream Chl. The eastern origin of water masses during both events (Figure 2b) indicates that waters were likely phosphate rich but nitrate and iron depleted (Bonnet et al., 2017; Moutin et al., 2008). Islands must have thus supplied at least nitrate and/or iron to support the Chl increase.

Islands can supply nutrients through several processes, including wind-driven coastal upwelling, uplifting and mixing in lee eddies, land runoff, atoll lagoon flushing, coral reef benthic processes, and iron enrichment from the island platform (Gove et al., 2016; Hasegawa et al., 2009; Palacios, 2002; Signorini et al., 1999). No correspondence was found between ΔChl and sea surface temperature, waves, or tides, so upwelling and lagoon flushing were unlikely. Island runoff was a possibility since both classical IMEs coincided with precipitation events (Figure 2c). The Tonga Islands considered here (part of the Vava'u and Ha'apai groups) are mostly low volcanic coral islands, but Vava'u slopes up to 200-m high cliffs in the north and rain could trigger significant runoff. However, not all precipitation events coincided with a Chl increase near the islands. Precipitation may thus be a necessary, but not sufficient, condition to trigger a classical IME. Surface currents and ΔChl are significantly correlated ($r = 0.56$ with a lag of 4–6 days and $p << 0.01$), and delayed bloom water mass origin coincides with strong currents (Figure 2d diamonds), supporting the hypothesis of an additional iron source related to currents.

### 3.2. Biological Evolution Following Island Fertilization

The temporal evolution of satellite Chl downstream of Tonga along the Lagrangian trajectories (Figure S1) clearly displays the classical IME in a significant number of trajectories, peaking within a few days. Interestingly, Chl usually displayed a second, separate peak weeks later. No significant water mass cooling was observed, so additional vertical nutrient inputs were unlikely. We propose that the two successive plankton blooms were supported by the same island-driven nutrient supply, indicating that two phytoplankton types responded to island fertilization with different time lags. *Trichodesmium* grow slower than most
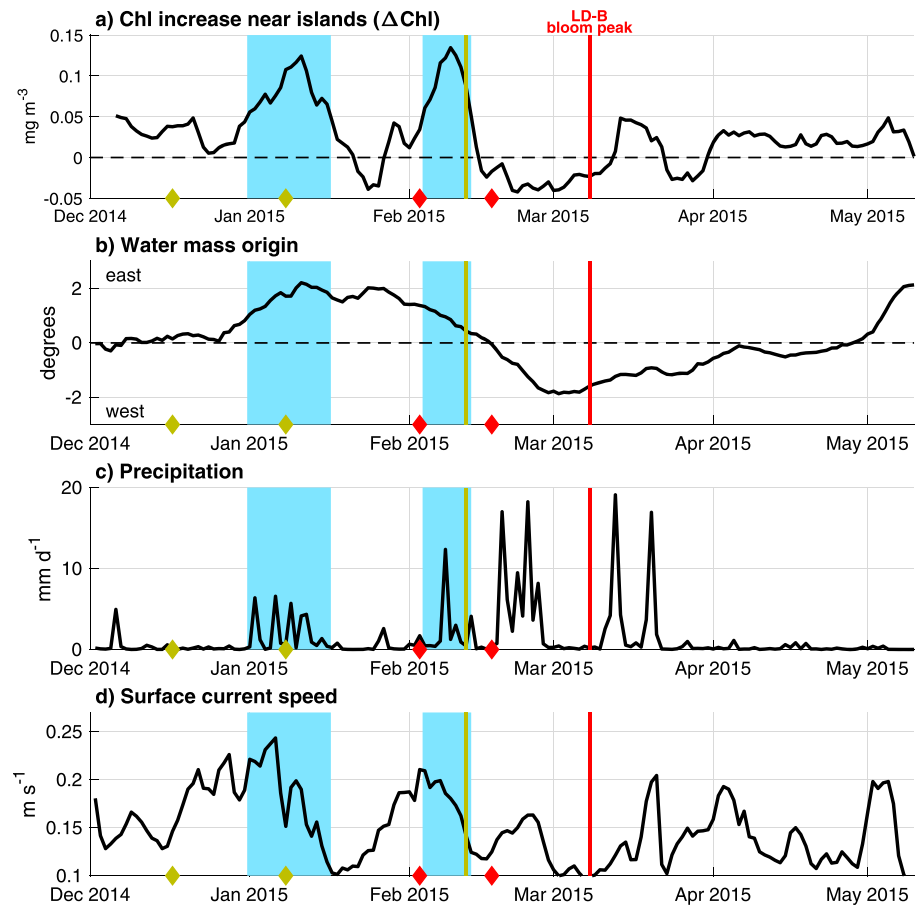
**Figure 2.** Characterization of the Tonga classical IME and its potential drivers. All variables were averaged over the 15-km Tonga region. Blue shading highlight times of significant Chl increase near islands, defined as $\Delta$Chl > 0.05 mg m$^{-3}$. The red line marks the LD-B bloom peak, and red diamonds circumscribe the period when 80% of its island-origin water masses* traveled through the 15-km Tonga region (*defined as along-trajectory satellite Chl > 0.7 mg m$^{-3}$ within 2 days of the bloom peak in the LD-B region; Figure S3). Dark yellow similarly displays the delayed SW bloom peak and origin (see section 3.3).

phytoplankton (Capone et al., 1997) and were thus likely responsible for the second bloom (delayed IME), as observed at LD-B (Bonnet et al., 2018). The first bloom (classical IME) was likely supported by nondiazotrophic phytoplankton because another diazotroph species would have consumed all available phosphate and iron, preventing the delayed bloom from occurring.

The plankton model was used to represent the temporal evolution of nondiazotrophic phytoplankton (*Phy*) and *Trichodesmium* (*Tri*) after an initial supply of nutrients (Figures 3a and 3b). The model represents a classical IME paradigm where *Phy* blooms within a few days. Nitrate exhaustion and predation terminate this early bloom after about 1 week. The model additionally predicts a separate, *Tri*-dominated later peak: the delayed IME. It occurs because *Tri* grows slowly and utilizes leftover phosphate and iron over several weeks. A secondary *Phy* peak is also observed around the *Tri* maximum, supported by nutrients released by *Tri* that, in turn, reenhance the bloom. Similar biological production enhancements due to *Trichodesmium* nutrient release have been observed previously (Bonnet et al., 2016; Caffin, Berthelot, et al., 2018). Once phosphate and/or iron stress become too high, the PCD causes the *Tri* bloom to collapse.

When considering advection by surface currents, the early and late Chl maxima translate into a peak near the islands (classical IME) and peaks in several locations away from the islands (delayed IME), respectively (Figure 3c). Not all trajectories display both an early and a late Chl peak, consistent with satellite observations (Figure S1). This is because *Phy* and *Tri* are decoupled in the model, *Phy* being primarily a function
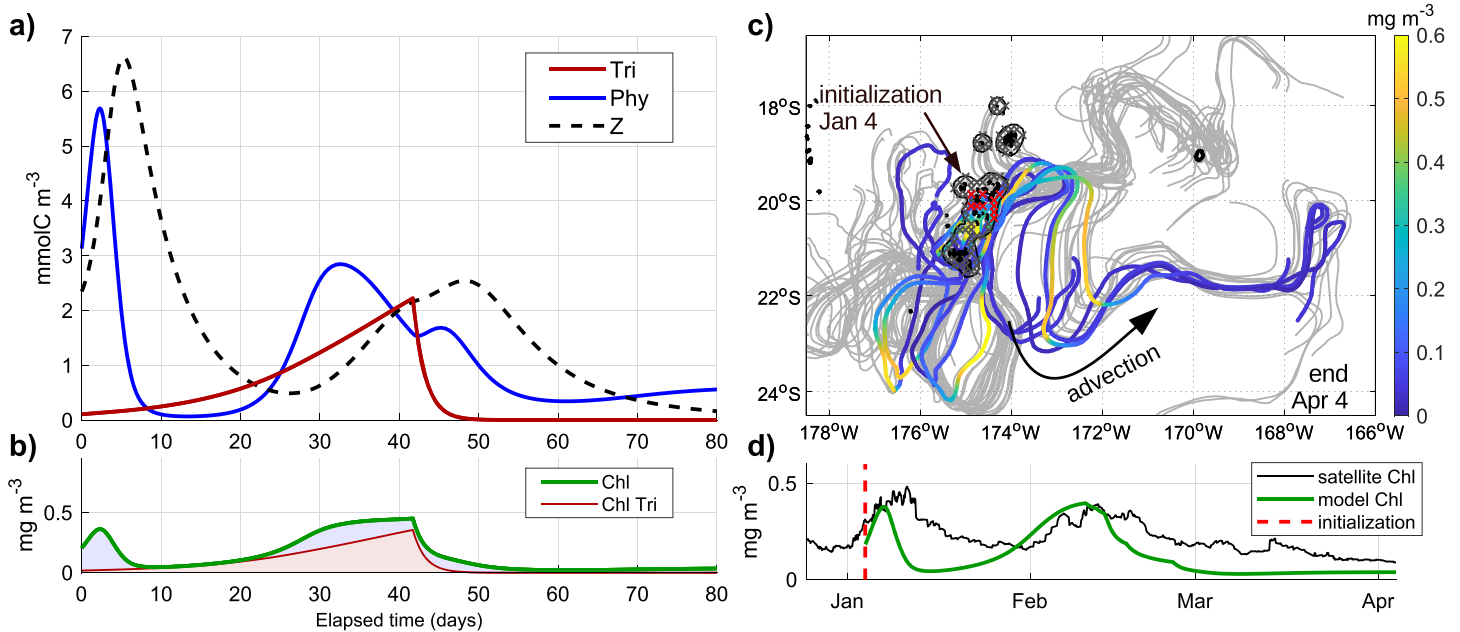
**Figure 3.** Example of plankton model output (left) and growth-advection run initialized on 4 January 2015 (right). (a) Modeled plankton biomass as a function of time, following initialization corresponding to median conditions at the red crosses in (c). (b) Corresponding modeled Chl, total (green line), and of *Tri* (dark-red line). Both the intensity and timing of the two Chl peaks depend on initial conditions. (c) Ninety-day forward trajectories (gray or color) initialized at gray and red crosses near the Tonga Islands. Along-trajectory modeled Chl is displayed in color for a few example trajectories initialized at the red crosses (between 19° and 20.5° S for $\Delta$Chl > 0.05 mg m$^{-3}$ and currents > 0.2 m s$^{-1}$). (d) Time series of modeled (green) and observed (black) along-trajectory Chl, averaged for the example trajectories. The shape of the modeled delayed Chl peak is different in (d) than (b) because its timing differs across the trajectories being averaged in (d) due to varying initial conditions. See Texts S1 and S2 regarding underestimated Chl in nonbloom conditions.

of $\Delta$Chl [controlling N(0)] and *Tri* of currents and water mass origin [controlling Fe(0) and excess P relative to N, respectively]. The modeled Chl peak timing is close to the timing of early and late peaks observed in satellite along-trajectory Chl (Figure 3d). *Tri*'s slow growth rate is thus responsible for the temporal decoupling between island fertilization and delayed IME, while advection by surface currents explains their spatial decoupling.

### 3.3. Classical and Delayed IME Impacts on Phytoplankton

Time-varying satellite Chl maps highlight several major blooms during the period of study (Figure 4, see also Movie S1): east (E) bloom close to Tonga in January, southwest (SW) bloom downstream of Tonga in mid-February, and LD-B bloom early March. These are separate from near-island Chl increases depicted in Figure 2 (blue shading). Island-driven Chl enrichments were examined by combining individual growth-advection daily runs (e.g., Figure 3c) into gridded daily maps. The result is remarkably similar to satellite Chl (Figures 3d, 4, and S3), requiring only island fertilization and oceanic advection to reproduce major bloom timing and spatial features. Using the *Tri–Phy* dominance as an indicator of delayed versus classical IME, the model identifies the E bloom as a classical IME and the SW and LD-B blooms as delayed IMEs. These represent two different situations: the SW bloom remained connected to the islands as water masses recirculated towards Tonga, while the LD-B bloom became separated as water masses got advected away. Both were preceded by island-driven fertilization and a classical IME by about 1 month (Figure 2a).

The model's success in representing satellite Chl has two implications. First, island-driven nutrient supply and oceanic advection are sufficient to reproduce the LD-B bloom, supporting the hypothesis that the bloom was a delayed IME fertilized by the Tonga Islands. Second, the growth-advection model represents all satellite-detected blooms, indicating that they were likely triggered by island effects. This suggests that islands were not only responsible for the LD-B bloom but even more remarkably were the primary driver of Chl variability in the region for the period of study. Island-driven iron inputs, in addition to submarine hydrothermal iron sources (Guieu et al., 2018), may thus contribute to explain the hotspot of nitrogen
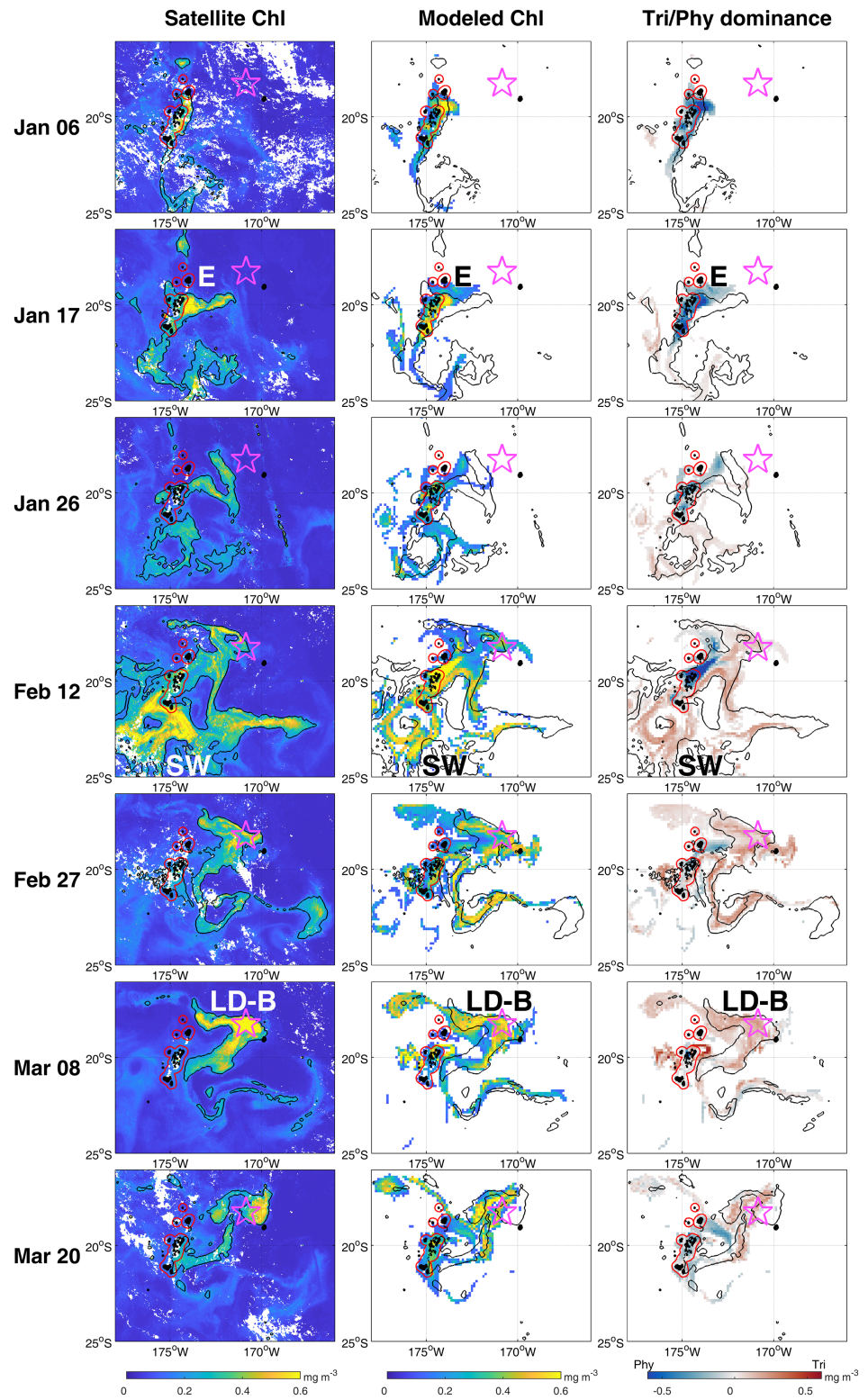
**Figure 4.** Chl temporal evolution as observed from satellite and modeled using the growth-advection method (see also Movie S1). Left: daily satellite Chl. Middle: model output, keeping only pixels where modeled Chl > 0.1 mg m$^{-3}$. Right: *Tri–Phy* dominance defined as *Tri* Chl minus *Phy* Chl, also representing the classical (*Phy* dominated, blue) versus delayed (*Tri* dominated, red) IMEs. In all panels, black contours represent the 0.2-mg m$^{-3}$ Chl contour from the satellite smoothed product, red contours encircle the 15-km Tonga region, and the pink star is the LD-B location.

fixation found in the western tropical South Pacific (Bonnet et al., 2017). Indeed, top 30-m iron concentrations along the OUTPACE transect were highest around the Tonga Islands ($0.98 \pm 0.16$ nM), an area where deeper concentrations were relatively low ($0.59 \pm 0.21$ nM) (Guieu et al., 2018).

The prevalence of delayed IMEs is difficult to quantify beyond the region and period of study. A detailed Lagrangian analysis, as performed here, would be needed to determine if an open-ocean bloom was fueled by island effects or by local processes. Our analysis required daily high-resolution Chl and current satellite products that were specifically produced for OUTPACE and are unfortunately not available on a regular basis. Nevertheless, an analysis of VIIRS chlorophyll near Tonga does suggest that delayed IMEs may be common in the region, particularly in summer (Figure S4). More generally, delayed IMEs may occur when conditions support diazotrophy (warm temperatures and stratified waters) in the presence of islands supplying iron and/or phosphate. Regions such as Melanesia's eastern boundary (i.e., Fiji and Tonga Islands) appear particularly favorable, as westbound phosphate-rich waters intersect volcanic, iron-rich islands.

Regardless of their frequency, delayed IMEs can be responsible for unusually strong phytoplankton blooms in a largely oligotrophic environment. At the peak of the two delayed IMEs described here, Chl reached values close to 1 mg m$^{-3}$, a tenfold increase relative to background concentrations. While classical IMEs can reach similar concentrations, the duration and spatial extent of delayed IMEs were much higher in the model (Figures 3 and 4). Summing the corresponding modeled Chl over space and time, delayed IMEs were responsible for enrichments ($>0.1$ mg m$^{-3}$) over twice as high as those of classical IMEs, even though classical IMEs were overestimated (Figure S3).

## 4. Conclusion

This study provides strong evidence for the existence of delayed IMEs, a previously undescribed type of island effect where the bloom is spatially and temporally decoupled from island fertilization. Contrary to classical IMEs where phytoplankton respond quickly, resulting in a bloom near an island, delayed IMEs are supported by slow-growing nitrogen fixers such as *Trichodesmium*. They can occur when conditions are favorable for diazotrophy (e.g., warm stratified waters), and excess iron and phosphate remain in water masses after a classical IME.

Delayed IMEs represent situations where the time scale for biology (weeks) is much longer than the advection time scale (days), which is very unusual in the ocean and results in a temporal and spatial decoupling between nutrient supply processes and phytoplankton response. Such a mismatch between biological and physical time scales can lead to unexpected blooms in stratified waters with no apparent origin. In particular, delayed IMEs do not match the classical IME definition of Chl increase nearby islands and would not be identified by traditional IME detection methods such as a Chl contour (Shiozaki et al., 2014) or an inverse relationship between Chl and distance to an island (Gove et al., 2016). Without in situ subsurface data revealing the lack of vertical processes, these remote blooms could be mistakenly attributed to (sub)-mesoscale activity. Island effects on phytoplankton biomass and productivity may thus have been largely underestimated.

## References

Behrenfeld, M. J., & Boss, E. S. (2014). Resurrecting the ecological underpinnings of ocean plankton blooms. *Annual Review of Marine Science*, 6, 167–194. https://doi.org/10.1146/annurev-marine-052913-021325

Berman-Frank, I., Bidle, K., Haramaty, L., & Falkowski, P. G. (2004). The demise of the marine cyanobacterium, Trichodesmium spp., via an autocatalyzed cell death pathway. *Limnology and Oceanography*, 49, 997–1005. https://doi.org/10.4319/lo.2004.49.4.0997

Berman-Frank, I., Cullen, J. T., Shaked, Y., Sherrell, R. M., & Falkowski, P. G. (2001). Iron availability, cellular iron quotas, and nitrogen fixation in Trichodesmium. *Limnology and Oceanography*, 46(6), 1249–1260. https://doi.org/10.4319/lo.2001.46.6.1249

Blain, S., Sarthou, G., & Laan, P. (2008). Distribution of dissolved iron during the natural iron-fertilization experiment KEOPS (Kerguelen Plateau, Southern Ocean). *Deep Sea Research Part II: Topical Studies in Oceanography*, 55(5-7), 594–605. https://doi.org/10.1016/j.dsr2.2007.12.028

Blanke, B., & Raynaud, S. (1997). Kinematics of the Pacific Equatorial Undercurrent: An Eulerian and Lagrangian approach from GCM results. *Journal of Physical Oceanography*, 27(6), 1038–1053. https://doi.org/10.1175/1520-0485(1997)027<1038:KOTPEU>2.0.CO;2

Bonnet, S., Berthelot, H., Turk-Kubo, K., Cornet-Barthaux, V., Fawcett, S., Berman-Frank, I., et al. (2016). Diazotroph derived nitrogen supports diatom growth in the South West Pacific: A quantitative study using nanoSIMS. *Limnology and Oceanography*, 61(5), 1549–1562. https://doi.org/10.1002/lno.10300

Bonnet, S., Caffin, M., Berthelot, H., Grosso, O., Benavides, M., Helias-Nunige, S., et al. (2018). In-depth characterization of diazotroph activity across the western tropical South Pacific hotspot of N2 fixation (OUTPACE cruise). *Biogeosciences*, 15(13), 4215–4232. https://doi.org/10.5194/bg-15-4215-2018

Bonnet, S., Caffin, M., Berthelot, H., & Moutin, T. (2017). Hot spot of N2 fixation in the western tropical South Pacific pleads for a spatial decoupling between N2 fixation and denitrification. *Proceedings of the National Academy of Sciences*, *114*(14), E2800–E2801. https://doi.org/10.1073/pnas.1619514114

Caffin, M., Berthelot, H., Cornet-Barthaux, V., Barani, A., Bonnet, S., & S. (2018). Transfer of diazotroph-derived nitrogen to the planktonic food web across gradients of N2 fixation activity and diversity in the western tropical South Pacific Ocean. *Biogeosciences*, *15*(12), 3795–3810. https://doi.org/10.5194/bg-15-3795-2018

Caffin, M., Moutin, T., Foster, R. A., Bouruet-Aubertot, P., Doglioli, A. M., Berthelot, H., et al. (2018). N2 fixation as a dominant new N source in the western tropical South Pacific Ocean (OUTPACE cruise). *Biogeosciences*, *15*(8), 2565–2585. https://doi.org/10.5194/bg-15-2565-2018

Capone, D. G., Zehr, J. P., Paerl, H. W., Bergman, B., & Carpenter, E. J. (1997). Trichodesmium, a globally significant marine cyanobacterium. *Science*, *276*(5316), 1221–1229. https://doi.org/10.1126/science.276.5316.1221

de Verneil, A., Rousselet, L., Doglioli, A. M., Petrenko, A. A., & Moutin, T. (2017). The fate of a southwest Pacific bloom: Gauging the impact of submesoscale vs. mesoscale circulation on biological gradients in the subtropics. *Biogeosciences*, *14*(14), 3471–3486. https://doi.org/10.5194/bg-14-3471-2017

Dore, J. E., Letelier, R. M., Church, M. J., Lukas, R., & Karl, D. M. (2008). Summer phytoplankton blooms in the oligotrophic North Pacific subtropical gyre: Historical perspective and recent observations. *Progress in Oceanography*, *76*(1), 2–38. https://doi.org/10.1016/j.pocean.2007.10.002

Doty, M. S., & Oguri, M. (1956). The island mass effect. *Journal du Conseil / Conseil Permanent International pour l'Exploration de la Mer*, *22*(1), 33–37. https://doi.org/10.1093/icesjms/22.1.33

Gove, J. M., McManus, M. A., Neuheimer, A. B., Polovina, J. J., Drazen, J. C., Smith, C. R., et al. (2016). Near-island biological hotspots in barren ocean basins. *Nature Communications*, *7*(1), 10581. https://doi.org/10.1038/ncomms10581

Guieu, C., Bonnet, S., Petrenko, A., Menkes, C., Chavagnac, V., Desboeufs, C., et al. (2018). Iron from a submarine source impacts the productive layer of the Western Tropical South Pacific (WTSP). *Scientific Reports*, *8*(1), 1–9. https://doi.org/10.1038/s41598-018-27407-z

Hasegawa, D., Lewis, M. R., & Gangopadhyay, A. (2009). How islands cause phytoplankton to bloom in their wakes. *Geophysical Research Letters*, *36*, L20605. https://doi.org/10.1029/2009GL039743

Huffman, G. J., Stocker, E. F., Bolvin, D. T., Nelkin, E. J., & Tan, J. (2019). GPM IMERG final precipitation L3 1 day 0.1 degree x 0.1 degree V06, Edited by Andrey Savtchenko, Greenbelt, MD, Goddard Earth Sciences Data and Information Services Center (GES DISC), Accessed: 05/27/2019, doi:https://doi.org/10.5067/GPM/IMERGDF/DAY/06

Johnson, K. S., Riser, S. C., & Karl, D. M. (2010). Nitrate supply from deep to near-surface waters of the North Pacific subtropical gyre. *Nature*, *465*(7301), 1062–1065. https://doi.org/10.1038/nature09170

Lehahn, Y., Koren, I., Sharoni, S., d'Ovidio, F., Vardi, A., & Boss, E. (2017). Dispersion/dilution enhances phytoplankton blooms in low-nutrient waters. *Nature Communications*, *8*, 14868. https://doi.org/10.1038/ncomms14868

Mahadevan, A. (2016). The impact of submesoscale physics on primary productivity of plankton. *Annual Review of Marine Science*, *8*(1), 161–184. https://doi.org/10.1146/annurev-marine-010814-015912

Martinez, E., & Maamaatuaiahutapu, K. (2004). Island mass effect in the Marquesas Islands: Time variation. *Geophysical Research Letters*, *31*, L18307. https://doi.org/10.1029/2004GL020682

McGillicuddy, D. J. J., Laurence, A. A., Bates, N. R., Bibby, T., Buesseler, K. O., Carlson, C. A., et al. (2007). Eddy/wind interactions stimulate extraordinary mid-ocean plankton blooms. *Science*, *316*(5827), 1021–1026. https://doi.org/10.1126/science.1136256

Menkes, C. E., Lengaigne, M., Lévy, M., Ethé, C., Bopp, L., Aumont, O., et al. (2016). Global impact of tropical cyclones on primary production. *Global Biogeochemical Cycles*, *30*(5), 767–786. https://doi.org/10.1002/2015GB005214

Messié, M., & Chavez, F. P. (2017). Nutrient supply, surface currents, and plankton dynamics predict zooplankton hotspots in coastal upwelling systems. *Geophysical Research Letters*, *44*(17), 8979–8986. https://doi.org/10.1002/2017GL074322

Messié, M., Radenac, M.-H., Lefèvre, J., & Marchesiello, P. (2006). Chlorophyll bloom in the western Pacific at the end of the 1997-98 El Niño: The role of the Kiribati Islands. *Geophysical Research Letters*, *33*, L14601. https://doi.org/10.1029/2006GL026033

Moosdorf, N., Stieglitz, T., Waska, H., Dürr, H. H., & Hartmann, J. (2015). Submarine groundwater discharge from tropical islands: A review. *Grundwasser*, *20*(1), 53–67. https://doi.org/10.1007/s00767-014-0275-3

Moutin, T., Doglioli, A. M., de Verneil, A., & Bonnet, S. (2017). Preface: The Oligotrophy to the UlTra-oligotrophy PACific Experiment (OUTPACE cruise, 18 February to 3 April 2015). *Biogeosciences*, *14*(13), 3207–3220. https://doi.org/10.5194/bg-14-3207-2017

Moutin, T., Karl, D. M., Duhamel, S., Rimmelin, P., Raimbault, P., Van Mooy, B. A. S., & Claustre, H. (2008). Phosphate availability and the ultimate control of new nitrogen input by nitrogen fixation in the tropical Pacific Ocean. *Biogeosciences*, *5*(1), 95–109. https://doi.org/10.5194/bg-5-95-2008

Moutin, T., Wagener, T., Caffin, M., Fumenia, A., Gimenez, A., Baklouti, M., et al. (2018). Nutrient availability and the ultimate control of the biological carbon pump in the western tropical South Pacific Ocean. *Biogeosciences*, *15*(9), 2961–2989. https://doi.org/10.5194/bg-15-2961-2018

Palacios, D. M. (2002). Factors influencing the island-mass effect of the Galapagos archipelago. *Geophysical Research Letters*, *29*(23), 2134. https://doi.org/10.1029/2002GL016232

Raapoto, H., Martinez, E., Petrenko, A. A., Doglioli, A. M., Gorgues, T., Sauzède, R., et al. (2019). Role of iron in the remarkable Marquesas island mass effect. *Journal of Geophysical Research, Oceans*, *124*(11), 7781–7796. https://doi.org/10.1029/2019JC015275

Rousselet, L., de Verneil, A., Doglioli, A. M., Petrenko, A. A., Duhamel, S., Maes, C., & Blanke, B. (2018). Large- to submesoscale surface circulation and its implications on biogeochemical/biological horizontal distributions during the OUTPACE cruise (southwest Pacific). *Biogeosciences*, *15*(8), 2411–2431. https://doi.org/10.5194/bg-15-2411-2018

Ryan, P. R., Polito, P. S., Strutton, P. G., & Chavez, F. P. (2002). Unusual large-scale phytoplankton blooms in the equatorial Pacific. *Progress in Oceanography*, *55*(3-4), 263–285. https://doi.org/10.1016/S0079-6611(02)00137-4

Shiozaki, T., Kodama, T., & Furuya, K. (2014). Large-scale impact of the island mass effect through nitrogen fixation in the western South Pacific Ocean. *Geophysical Research Letters*, *41*(8), 2907–2913. https://doi.org/10.1002/2014GL059835

Signorini, S. C., McClain, C. R., & Dandonneau, Y. (1999). Mixing and phytoplankton bloom in the wake of the Marquesas Islands. *Geophysical Research Letters*, *26*(20), 3121–3124. https://doi.org/10.1029/1999GL010470

Spungin, D., Belkin, N., Foster, R. A., Stenegren, M., Caputo, A., Pujo-Pay, M., et al. (2018). Programmed cell death in diazotrophs and the fate of organic matter in the western tropical South Pacific Ocean during the OUTPACE cruise. *Biogeosciences*, *15*(12), 3893–3908. https://doi.org/10.5194/bg-15-3893-2018

Wilson, C., & Qiu, X. (2008). Global distribution of summer chlorophyll blooms in the oligotrophic gyres. *Progress in Oceanography*, *78*(2), 107–134. https://doi.org/10.1016/j.pocean.2008.05.002

Wilson, C., Villareal, T. A., Maximenko, N., Bograd, S. J., Montoya, J. P., & Schoenbaechler, C. A. (2008). Biological and physical forcings of late summer chlorophyll blooms at 30N in the oligotrophic Pacific. *Journal of Marine Systems*, *69*(3-4), 164–176. https://doi.org/10.1016/j.jmarsys.2005.09.018

## References From the Supporting Information

Alessandri, A., & Parisini, T. (1997). Nonlinear modeling of complex large-scale plants using neural networks and stochastic approximation. *IEEE Transactions on Systems, Man, and Cybernetics-Part A: Systems and Humans*, *27*(6), 750–757. https://doi.org/10.1109/3468.634638

Altaf, M. U., Heemink, A. W., Verlaan, M., & Hoteit, I. (2011). Simultaneous perturbation stochastic approximation for tidal models. *Ocean Dynamics*, *61*(8), 1093–1105. https://doi.org/10.1007/s10236-011-0387-6

Breitbarth, E., Wohlers, J., Kläs, J., LaRoche, J., & Peeken, I. (2008). Nitrogen fixation and growth rates of Trichodesmium IMS-101 as a function of light intensity. *Marine Ecology Progress Series*, *359*, 25–36. https://doi.org/10.3354/meps07241

Chin, D. C. (1998). The simultaneous perturbation method for processing magnetospheric images, *Proceedings of the 1998 IEEE International Symposium on Intelligent Control (ISIC) held jointly with IEEE International Symposium on Computational Intelligence in Robotics and Automation (CIRA) Intell* (pp. 616-621), IEEE, https://doi.org/10.1117/1.602104

Dupouy, C., Frouin, R., Tedetti, M., Maillard, M., Rodier, M., Lombard, F., et al. (2018). Diazotrophic Trichodesmium impact on UV-Vis radiance and pigment composition in the western tropical South Pacific. *Biogeosciences*, *15*(16), 5249–5269. https://doi.org/10.5194/bg-15-5249-2018

Dutheil, C., Aumont, O., Gorguès, T., Lorrain, A., Bonnet, S., Rodier, M., et al. (2018). Modelling N2 fixation related to Trichodesmium sp.: Driving processes and impacts on primary production in the tropical Pacific Ocean. *Biogeosciences*, *15*(14), 4333–4352. https://doi.org/10.5194/bg-15-4333-2018

Fasham, M. J. R., Ducklow, H. W., & McKelvie, S. M. (1990). A nitrogen-based model of plankton dynamics in the oceanic mixed layer. *Journal of Marine Research*, *48*(3), 591–639. https://doi.org/10.1357/002224090784984678

Fu, F.-X., Zhang, Y., Bell, P. R. F., & Hutchins, D. A. (2005). Phosphate uptake and growth kinetics of Trichodesmium (cyanobacteria) isolates from the North Atlantic Ocean and the Great Barrier Reef, Australia. *Journal of Phycology*, *41*(1), 62–73. https://doi.org/10.1111/j.1529-8817.2005.04063.x

Glibert, P. M., & Bronk, D. A. (1994). Release of dissolved organic nitrogen by marine diazotrophic cyanobacteria, Trichodesmium spp. *Applied and Environmental Microbiology*, *60*(11), 3996–4000.

Ruder, S. (2016). An overview of gradient descent optimization algorithms, *arXiv preprint* arXiv:1609.04747, https://arxiv.org/abs/1609.04747

Spall, J. (1998). An overview of the simultaneous perturbation method for efficient optimization. *Johns Hopkins APL Technical Digest*, *19*(5), 482–492.

Spall, J. (2012), Stochastic optimization. In J. Gentle, W. Härdle, and Y. Mori, (eds.) *Handbook of computational statistics: Concepts and methods* (2nd ed.), Springer-Verlag, Heidelberg, Chap 7, pp. 173-201.

Spall, J. C., & Cristion, J. A. (1994). Nonlinear adaptive control using neural networks: Estimation with a smoothed form of simultaneous perturbation gradient approximation, *Proceedings of 1994 American Control Conference-ACC'94* (Vol. 3, pp. 2560-2564), IEEE, https://doi.org/10.1109/ACC.1994.735021

Tympakianaki, A., Koutsopoulos, H. N., & Jenelius, E. (2015). c-SPSA: Cluster-wise simultaneous perturbation stochastic approximation algorithm and its application to dynamic origin–destination matrix estimation. *Transportation Research Part C: Emerging Technologies*, *55*. https://doi.org/10.1016/j.trc.2015.01.016

Ye, Y., Völker, C., Bracher, A., Taylor, B., & Wolf-Gladrow, D. A. (2012). Environmental controls on N2 fixation by Trichodesmium in the tropical eastern North Atlantic Ocean-A model-based study. *Deep Sea Research Part I: Oceanographic Research Papers*, *64*, 104–117. https://doi.org/10.1016/j.dsr.2012.01.004

**The Delayed Island Mass Effect: how islands can remotely trigger blooms in the oligotrophic ocean**

M. Messié[1,2,*], A. Petrenko[1], A.M. Doglioli[1], C. Aldebert[1],
E. Martinez[3], G. Koenig[1], S. Bonnet[1], and T. Moutin[1]

[1]Aix Marseille Université, Université de Toulon, CNRS, IRD, Mediterranean Institute of Oceanography (MIO), Unité Mixte 110, 13288 Marseille, France,
[2]Monterey Bay Aquarium Research Institute, Moss Landing, CA 95039, USA,
[3]University of Brest, Ifremer, CNRS, IRD, Laboratoire d'Océanographie Physique et Spatiale (LOPS), IUEM, 29200 Brest, France,
[*]corresponding author, monique@mbari.org

## Contents of this file

## Additional Supporting Information (Files uploaded separately)

## Introduction

This file contains supplementary information regarding:
- along-trajectory satellite chlorophyll (Figure S1);
- the plankton model and its initialization, including the model schematic (Figure S2), the model description and full equations (Text S1), the model parameters fixed based on literature values (Table S1), the optimized model and initialization parameters before and after optimization (Table S2), and a validation of the model output at LD-B against in situ data (Table S3);
- the optimization method, including information on the cost function definition and algorithm used (Text S2), and the optimization results (Figure S3);
- the prevalence of delayed IMEs in the VIIRS satellite chlorophyll record (Figure S4);
- the full model output, as a movie (uploaded separately).

**Text S1.**

The model is a simplified version of plankton models such as developed by Fasham et al. (1990), and more precisely builds upon the Messié & Chavez (2017) plankton model by only considering one type of phytoplankton (*Phy*) and zooplankton (*Z*), but adding diazotrophic phytoplankton (*Trichodesmium Tri*) and representing the nutrients N, P and Fe instead of $NO_3$ and $NH_4$. Detritus and bacteria are not explicitly represented. The model was intentionally kept as simple as possible while still being able to correctly represent the bloom and its timing.

The real phytoplankton community is of course more complex, including several diazotrophic and non-diazotrophic species. According to OUTPACE pigment measurements, the phytoplankton community at LD-B was dominated by *Trichodesmium* (25% of Chl biomass) and by non-diazotrophic picoplankton such as *Prochlorococcus* (45%), *Synechococcus* + picoeukaryotes (7%) and nanoeukaryotes (5%) (Dupouy et al., 2018). Other phytoplankton species may be present particularly following nutrient supply near the Tonga islands (not sampled during OUTPACE). To limit complexity, only one non-diazotrophic phytoplankton species was represented (*Phy*), and parameterized based on *Prochlorococcus*. Similarly, while other diazotrophs were present, they were likely of secondary importance as *Trichodesmium* represented 91.8% of the diazotroph community (in terms of nifH copies $L^{-1}$) and 52.9% of bulk $N_2$ fixation (Bonnet et al., 2018). We did not aim for an entirely realistic model, notably because of the lack of information on phytoplankton community outside of the LD-B station and to keep the mode simple. In particular, non-bloom *Phy* concentrations are largely underestimated in the model (e.g., Fig. 3), due to the lack of a detritus pool and of nutrient supply processes after time 0 (except nitrogen fixation).

In the model (Fig. S2), fast-growing non-diazotrophic phytoplankton (*Phy*) take up all nutrients (Fe does not limit growth because iron requirement is low for non-diazotrophs) and are being grazed by zooplankton (*Z*), whose excretion releases nutrients. A quadratic death closure term is applied to *Z*, corresponding to export and transfer to higher trophic levels. Slow-growing *Trichodesmium* (*Tri*) take up Fe and P, release excess N when fixing nitrogen, and release all nutrients at death. *Tri* is not grazed in the model, as *Trichodesmium* is toxic for most grazers (Caffin et al., 2018b and references therein). However, the diazotroph-derived N does indirectly transfer to zooplankton via the dissolved pool and assimilation by non-diazotrophs, as observed by Caffin et al. (2018b). Another *Tri* characteristic in the model is the representation of a programmed cell death (PCD), a process by which *Trichodesmium* blooms can collapse within a few days in response to nutrient stress (see Spungin et al., 2018 for its investigation during OUTPACE). The PCD has not been modeled before to our knowledge; our simple implementation is based on two observations (Spungin et al., 2018 and references therein): (1) the PCD was likely triggered by nutrient stress, and (2) death rates during the PCD are similar to growth rates during the bloom. As such we simply implemented the PCD by stopping *Tri* growth and increasing its mortality to a given PCD mortality rate (initially set at the nutrient-replete growth rate), once the nutrient limitation term drops below a given threshold. Both the PCD mortality rate and nutrient stress threshold were optimized (Text S2), as they are not well constrained in the literature. It should be noted that the PCD may lead to a strong carbon export of *Trichodesmium* (Spungin et al., 2018); however, *Trichodesmium* represented < 5% of particulate carbon in sediment traps at LD-B, suggesting that nutrients accumulated in phytoplankton (including *Trichodesmium*) were released to the dissolved pool and quickly remineralized (Caffin et al., 2018a), as represented in our model.

Per its construction, the primary factors influencing the temporal separation between *Phy* and *Tri* and the existence of a separate delayed bloom are: (1) the difference between the *Phy* and *Tri* maximum growth rates, (2) parameters controlling *Z* grazing on *Phy* (which includes *Z*

loss terms as they decrease Z biomass), and (3) initial conditions, including both nutrients and biomass (which both impact how quickly *Phy* and *Tri* exhaust resources). Initial nutrient concentrations are described in text (section 2.2); initial plankton concentrations were constrained by *Phy*(0):*Z*(0) and *Phy*(0):*Tri*(0) ratios, and by having the modeled Chl(0) be equal to Chl_upstream. While *Phy*(0):*Z*(0) was fixed, *Phy*(0):*Tri*(0) evolved over time following the modeled *Phy/Tri* ratio averaged in the 15-km Tonga region (some Lagrangian trajectories turned back towards the islands, bringing *Tri*-rich waters there).

The full model equations are listed below. All concentrations and fluxes are C-based, except for nutrients. The corresponding parameters are given in Tables S1 and S2.

$\gamma_{Phy} = min\left(\frac{N}{k_N^{Phy}+N}, \frac{P}{k_P^{Phy}+P}\right)$ nutrient limitation for *Phy*

$\mu_{Phy} = \gamma_{Phy} * \mu_{max}^{Phy}$ growth rate for *Phy*

$\gamma_{Tri} = min\left(\frac{P}{k_P^{Tri}+P}, \frac{Fe}{k_{Fe}^{Tri}+Fe}\right)$ nutrient limitation for *Tri* (PCD starts when $\gamma_{Tri} < \gamma_{Tri}^{PCD}$)

$\mu_{Tri} = \gamma_{Tri} * \mu_{max}^{Tri}$ (normal) or $\mu_{Tri} = 0$ (PCD)  growth rate for *Tri*

$m_{Tri} = m_{normal}^{Tri}$ (normal) or $m_{Tri} = m_{PCD}^{Tri}$ (PCD)  mortality for *Tri*

$g = \frac{Phy}{k_G+Phy} * g_{max}$ grazing rate for *Z*

$PP_{Phy} = \mu_{Phy} * Phy$ primary production for *Phy*

$PP_{Tri} = \mu_{Tri} * Tri$ primary production for *Tri*

$G = g * Z$ *Z* grazing on *Phy*

$death_{Tri} = m_{Tri} * Tri$ *Tri* death

$death_Z = m_Z * Z^2$ *Z* death (closure term)

$excretion_{Tri} = fe_{Tri} * PP_{Tri}$ excretion *Tri* (N only, corresponds to excess N fixation)

$excretion_Z = e_Z * Z$ excretion *Z*

$\frac{dN}{dt} = (\varepsilon * excretion_Z + excretion_{Tri} + death_{Tri} - PP_{Phy}) * N{:}C$

$\frac{dP}{dt} = (\varepsilon * excretion_Z + death_{Tri} - PP_{Phy} - PP_{Tri}) * P{:}C$

$\frac{dFe}{dt} = (\varepsilon * excretion_Z + PP_{Phy}) * Fe{:}C_{Phy} + (death_{Tri} - PP_{Tri}) * Fe{:}C_{Tri}$

$\frac{dPhy}{dt} = PP_{Phy} - G$

$\frac{dTri}{dt} = PP_{Tri} - death_{Tri}$

$\frac{dZ}{dt} = G - excretion_Z - death_Z$

**Text S2.**

    **Optimization overview:** An optimization method was applied to model parameters, in order to improve the timing and magnitude of blooms by finding the set of model parameters that best represented satellite Chl. While most parameters can be constrained by the literature (Table S1, not optimized), several were unknown and were targeted by the optimization method (Table S2). We used a slightly modified version of the Simultaneous Perturbation Stochastic Approximation (SPSA) algorithm, a gradient-descent method developed by Spall (1998, 2012), that iteratively minimizes a scalar metrics representing the performance of a given parameter set (see "cost function" below). The optimization was initialized starting from a "first guess" set of parameters (Table S2), and optimized over several iterations by computing directional derivatives of the cost function in the parameter space and using those derivatives as gradient approximation for modifying the parameters (see "SPSA algorithm" below). At each iteration, the growth-advection model was run for two sets of slightly perturbed parameters. The cost of each corresponding model output was computed, and the cost function gradient estimated in parameter space. The SPSA algorithm then followed its slope downward to derive the next set of parameters, and the method was repeated until a local minimum was found.

    **Optimized parameters:** listed in Table S2.

    **Cost function:** The cost function was designed to optimize the model representation of delayed IMEs (timing and magnitude). It was defined as the sum of the RMS differences squared of modeled and satellite Chl averaged in 2 boxes where delayed IMEs were observed: around LD-B, and southwest of the islands (Fig. S3). Because modeled Chl is significantly lower than satellite Chl in non-bloom periods (Fig. 3d) and the goal was to best represent blooms, Chl values below 0.2 mg m$^{-3}$ were set to 0.2 before averaging, in order to keep most weight on high values. As a consequence, neither classical IMEs nor low Chl values were optimized.

    **SPSA algorithm:** The SPSA algorithm was chosen because it works well for optimizations characterized by heterogeneous parameters and non-linear relationships (Alessandri & Parasini, 1997), while remaining simple to implement. It has been successfully used in other fields (e.g., Altaf et al, 2011; Chin, 1998; Tympakianaki et al., 2015). The method approximates the gradient of the cost function by using only two model runs, randomly varying all the parameters being optimized together. This approximation still provides sufficient knowledge to perform optimization by quickly finding the cost function minimum. The optimization was performed on scaling values (applied to the first-estimate parameters) rather than on the parameters themselves, in order to avoid numerical issues related to parameter values of different magnitude. A few modifications were introduced relative to published applications (e.g., Spall, 2012). The decrease of gain and perturbation coefficients during iterations (Spall, 1998) were removed, as this reduces the number of needed iterations and thus increases efficiency. The perturbation coefficient (controlling the parameter perturbations used to estimate the cost function gradient) was adjusted to 1% and the gain coefficient (controlling the parameter set modifications as a function of the local cost function gradient) was adjusted to unity. This limited the maximal precision of the parameter set identification; however, precision is a trade-off for computing power, and considering the simplicity of the model (rough representation of satellite Chl expected) and the time needed for one growth-advection run computation (~ 10 min on a 3.6GHz, 3.9GHz turbo computer) we deemed computational power to be more important than precision. Finally, a momentum method that introduces a "gradient memory" was implemented for the gradient descent (Spall & Cristion, 1994), with the Nesterov technique (Ruder, 2016) and a momentum parameter of 0.8.

    **Results:** The optimization consisted of successive runs of 100 optimization steps, as the duration of the overall optimization was unknown *a priori*. It was manually sped up at times by

considering the trend of the parameter change with iterations and projecting future values. The optimization was iteratively run until the algorithm had fallen within the basin of attraction of a locally optimal parameter set. The final parameter set gave a cost function value of $4.1306\ 10^{-4}$, which represents a gain of 43.8% in comparison to the parameter set used as a first guess. The decrease of the cost function corresponds with a better timing of the bloom peaks and closer peak values (Fig. S3) although the SW bloom remains underestimated.
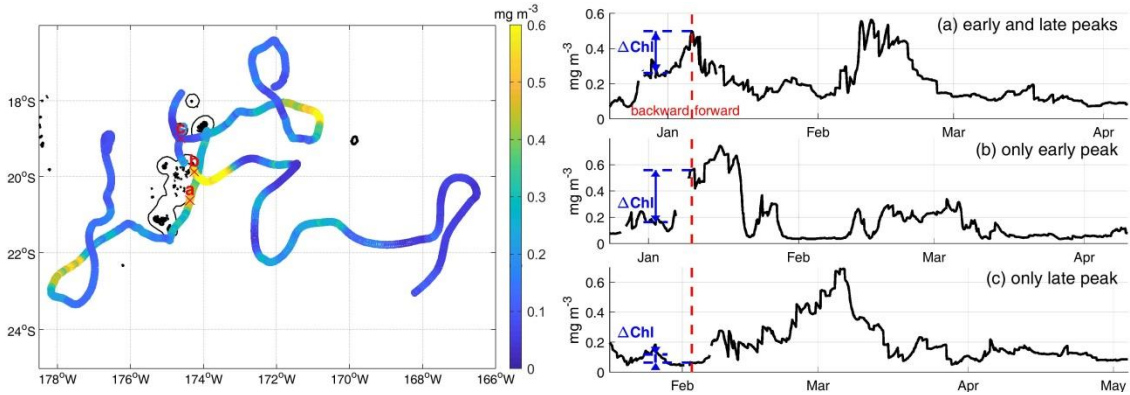
**Figure S1.** Examples of along-trajectory satellite Chl time series initialized near the Tonga islands. Three forward/backward trajectories are displayed, corresponding to situations where (a) both early and late peaks are observed, (b) no clear delayed peak was observed, and (c) only a delayed peak was observed. The early peak sometimes is seen at the islands as in (a), sometimes slightly downstream as in (b). The timing of the late peak also varies. In all time series, the initialization is represented with a red dashed line and ΔChl is represented in blue (difference between Chl near the islands and Chl 5-10 days upstream). The corresponding trajectories are displayed on the map (colors = satellite Chl). Note that the initialization days are different: (a) January 6th, (b) January 10th, and (c) February 3rd.
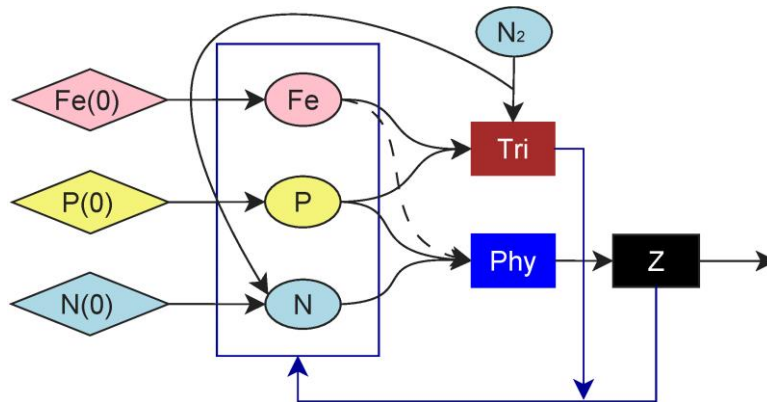


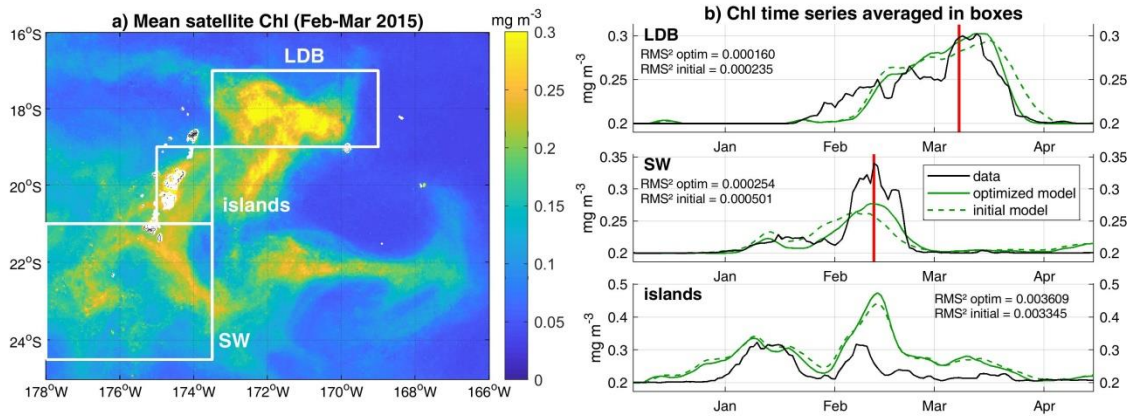**Figure S2.** Model schematic (see full description in Text S1).

6

**Figure S3.** Model optimization method and results. a) The model was optimized based on the sum of costs computed in the LD-B and SW boxes depicted in white (delayed IME regions). The cost of the initial model was 7.3542 10$^{-4}$, and of the optimized model 4.1306 10$^{-4}$ (43.8% improvement). The islands box was used to control that the classical IME was reasonably represented as well. b) For each box, the cost function was defined as the squared sum of RMS differences between the observed (black) and modeled (green) time series averaged in the box after setting all values below 0.2 mg m$^{-3}$ to 0.2, to focus on the correct representation of high concentrations. The corresponding values are given for each box (RMS$^2$). The red lines highlight the LD-B bloom peak (March 8th, 2015), and the SW bloom peak (February 12th, 2015). The optimization method improved the bloom timing in both cases. This is a result of the optimization automatically attempting to shift the timing to minimize the RMS difference between the two time series. The bloom magnitude was also improved.
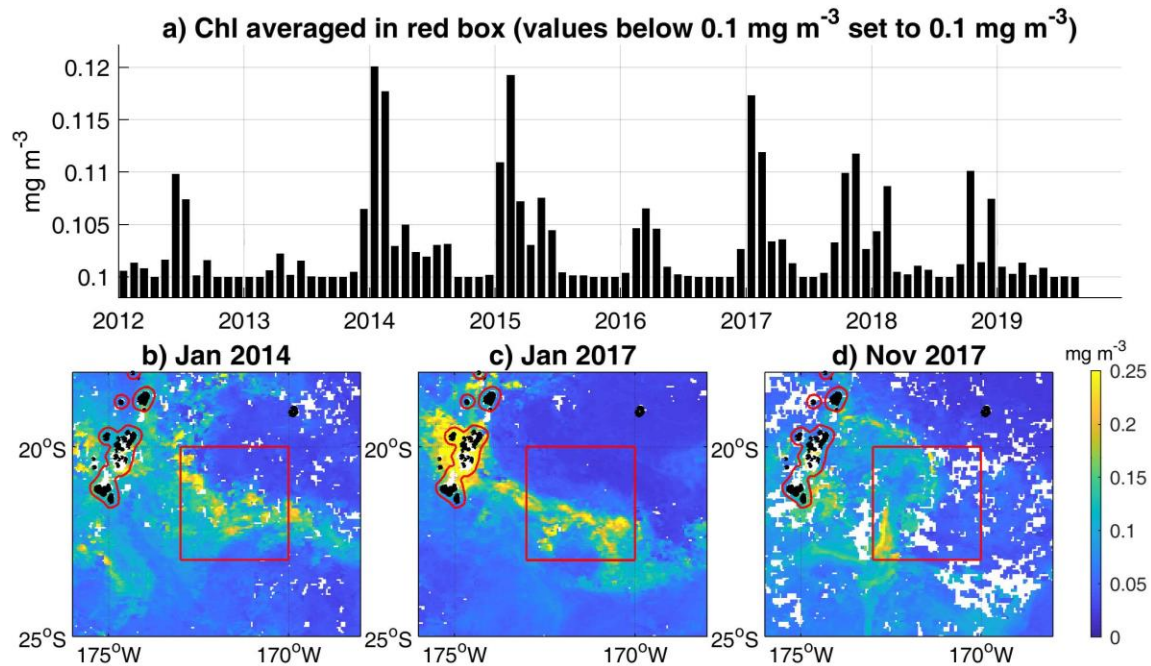
7

**a) Chl averaged in red box (values below 0.1 mg m$^{-3}$ set to 0.1 mg m$^{-3}$)**

**b) Jan 2014**  **c) Jan 2017**  **d) Nov 2017**

**Figure S4.** Analysis of potential delayed IMEs over the VIIRS time period (2012-present). Inspection of monthly satellite images suggest that delayed IMEs may be most common southeast of the Tonga islands (red box), and a time series of Chl in the region was computed as a potential index of delayed IME temporal frequency (Chl values below 0.1 mg m$^{-3}$ were set to 0.1 mg m$^{-3}$, otherwise regional changes in background concentrations dominate the signal). High values of the index suggest the occurrence of a delayed IME (examples below), although some blooms remain connected to the islands, suggesting a classical IME (summer 2012, not shown). A detailed analysis of each bloom, requiring daily high-resolution satellite data not available for the full time period, would be needed to conclusively attribute them to island effects rather than local processes. Nevertheless, the index suggests that delayed IMEs are more likely to be observed in austral summer, and display a strong interannual variability with strongest blooms observed in summers of 2014, 2015 and 2017.

| Parameter | Unit | Value | Reference |
|---|---|---|---|
| $k_N^{Phy}$ | mmolN m$^{-3}$ | 0.5 | Messié and Chavez (2017) |
| $k_P^{Phy}$ | mmolP m$^{-3}$ | 0.015 | Ye et al. (2012) |
| $k_P^{Tri}$ | mmolP m$^{-3}$ | 0.15 | Fu et al. (2005) |
| $k_{Fe}^{Tri}$ | mmolFe m$^{-3}$ | 0.75 *10$^{-3}$ | Ye et al. (2012) |
| $\mu_{max}^{Phy}$ | d$^{-1}$ | 1 | Dutheil et al. (2018) |
| $\mu_{max}^{Tri}$ | d$^{-1}$ | 0.27 | Breitbarth et al. (2008) |
| $\gamma_{Tri}^{PCD}$ | | 0.25 | Guess (no literature value) |
| $fe_{Tri}$ | | 1 | 50% of fixed N being released (Glibert and Bronk, 1994; Caffin et al, 2018b) |
| $k_G$ | mmolC m$^{-3}$ | 6.625 | 1 mmolN m$^{-3}$, Messié and Chavez (2017) |
| $g_{max}$ | d$^{-1}$ | 1 | Messié and Chavez (2017) |
| $m_Z$ | mmolC$^{-1}$ m$^3$ d$^{-1}$ | 7.5472*10$^{-3}$ | 0.05 mmolN$^{-1}$ m$^3$ d$^{-1}$, Messié and Chavez (2017) |
| $e_Z$ | d$^{-1}$ | 0.15 | Increased relative to Messié and Chavez (2017) |
| $\varepsilon$ | | 0.25 | Messié and Chavez (2017) |
| P:N:C | molP:molN:molC | 1:16:106 | Redfield ratios |
| $Fe:C_{Phy}$ | molFe:molC | 4*10$^{-5}$ | Dutheil et al. (2018) |
| $Fe:C_{Tri}$ | molFe:molC | 10$^{-4}$ | Dutheil et al. (2018) |
| $C:Chl_{Phy}$ | gC:gChl | 200 | Messié and Chavez (2017) |
| $C:Chl_{Tri}$ | gC:gChl | 75 | 70 in Ye et al. (2012) |

**Table S1.** Model parameters (except PCD-related parameters, see Table S2).

| Parameter | Initial value | Optimized value | Description |
|---|---|---|---|
| $\gamma_{Tri}^{PCD}$ | 0.25 | 0.287 | Nutrient limitation threshold triggering the PCD |
| $m_{PCD}^{Tri}$ | 0.25 | 0.631 | PCD mortality rate (d$^{-1}$) |
| distIles | 15 | 14.0 | Initialization zone (km) |
| upstreamP | 0.12 | 0.137 | Upstream P concentration (mmolP m$^{-3}$) when water masses originate from the east |
| k_Nsupply | 7 | 9.47 | Proportionality coefficient such that N(0)=ΔChl*k_Nsupply |
| k_Fesupply | 250 | 212.9 | Proportionality coefficient such that Fe(0)=curr/k_Fesupply |
| *Phy*(0):*Tri*(0) | 2 | 9.98 | Initial *Phy*:*Tri* ratio at t = 0 (later updated, see Text S1) |
| *Phy*(0):*Z*(0) | 3 | 1.33 | *Phy*:*Z* ratio at t = 0 |

**Table S2.** Initialization parameters (before and after optimization). The initial values were roughly tuned to represent the Chl variability before optimization.

| Parameter | Measured value | Modeled value | Modeled value (3-day shift) | Reference |
|---|---|---|---|---|
| Fe concentration | 0.71 nM | 0.97 nM | 0.94 nM | Guieu et al. (2018) |
| P concentration | < 0.05 µM | 0.08 µM | 0.09 µM | de Verneil et al. (2017) |
| Chl | 0.433 mg m$^{-3}$ | 0.29 mg m$^{-3}$ | 0.10 mg m$^{-3}$ | Dupouy et al. (2018) |
| *Trichodesmium* %Chl | 25% | 40.7% | 10.5% | Dupouy et al. (2018) |

**Table S3.** Model output validation using published OUTPACE data (Station LD-B). Modeled values are obtained by averaging the model output between March 15-20, 2015 over the four pixels closest to LD-B. Because the the bloom peak and demise are a few days late in the model (Fig. S3), a comparison with modeled values between March 18-23 (3-day shift) is also provided.


**Movie S1.** Bloom evolution as observed from satellite Chl and modeled with the growth-advection method (December 2nd, 2014 to April 15th, 2015 time period). Left: daily satellite Chl. Middle: model output, keeping only pixels where modeled Chl > 0.1 mg m-3. Right: *Tri-Phy* dominance defined as *Tri* Chl minus *Phy* Chl. This also represents the classical (*Phy*-dominated, blue) vs. delayed (*Tri*-dominated, red) IMEs. In all panels, black contours represent the 0.2 mg m$^{-3}$ Chl contour from the satellite smoothed product, red contours encircle the 15-km Tonga region, and the pink star is the LD-B location. The movie highlights three major blooms: E bloom mid-January, SW bloom mid-February, and LD-B bloom early March.

### References

Alessandri, A., & Parisini, T. (1997), Nonlinear modeling of complex large-scale plants using neural networks and stochastic approximation, *IEEE Transactions on Systems, Man, and Cybernetics-Part A: Systems and Humans*, 27(6), 750-757, https://doi.org/10.1109/3468.634638

Altaf, M. U., Heemink, A. W., Verlaan, M., & Hoteit, I. (2011). Simultaneous perturbation stochastic approximation for tidal models. Ocean Dynamics, 61(8), 1093-1105. https://doi.org/10.1007/s10236-011-0387-6

Bonnet, S., Caffin, M., Berthelot, H., Grosso, O., Benavides, M., Helias-Nunige, S., et al. (2018), In-depth characterization of diazotroph activity across the western tropical South Pacific hotspot of N2 fixation (OUTPACE cruise), Biogeosciences, 15(13), 4215-4232, https://doi.org/10.5194/bg-15-4215-2018

Breitbarth, E., Wohlers, J., Kläs, J., LaRoche, J., & Peeken, I. (2008), Nitrogen fixation and growth rates of Trichodesmium IMS-101 as a function of light intensity, *Mar. Ecol. Prog. Ser.*, *359*, 25-36, https://doi.org/10.3354/meps07241

Caffin, M., Berthelot, H., Cornet-Barthaux, V., Barani, A., & S. Bonnet, S. (2018b), Transfer of diazotroph-derived nitrogen to the planktonic food web across gradients of N2 fixation activity and diversity in the western tropical South Pacific Ocean, Biogeosciences, 15(12), 3795-3810, https://doi.org/10.5194/bg-15-3795-2018

Caffin, M., Moutin, T., Foster, R. A., Bouruet-Aubertot, P., Doglioli, A. M., Berthelot, H., et al. (2018a), N2 fixation as a dominant new N source in the western tropical South Pacific Ocean (OUTPACE cruise), Biogeosciences, 15(8), 2565-2585, https://doi.org/10.5194/bg-15-2565-2018

Chin, D. C. (1998), The simultaneous perturbation method for processing magnetospheric images, *Proceedings of the 1998 IEEE International Symposium on Intelligent Control (ISIC) held jointly with*

*IEEE International Symposium on Computational Intelligence in Robotics and Automation (CIRA) Intell* (pp. 616-621), IEEE, https://doi.org/10.1117/1.602104

Dupouy, C., Frouin, R., Tedetti, M., Maillard, M., Rodier, M., Lombard, F., et al. (2018), Diazotrophic Trichodesmium impact on UV-Vis radiance and pigment composition in the western tropical South Pacific, *Biogeosciences*, *15*(16), 5249-5269, https://doi.org/10.5194/bg-15-5249-2018

Dutheil, C., Aumont, O., Gorguès, T., Lorrain, A., Bonnet, S., Rodier, M., et al. (2018), Modelling N2 fixation related to Trichodesmium sp.: driving processes and impacts on primary production in the tropical Pacific Ocean, *Biogeosciences*, *15*(14), 4333-4352, https://doi.org/10.5194/bg-15-4333-2018

Fasham, M. J. R., Ducklow, H. W., & McKelvie, S. M. (1990), A nitrogen-based model of plankton dynamics in the oceanic mixed layer, J. Mar. Res., 48(3), 591-639, https://doi.org/10.1357/002224090784984678

Fu, F.-X., Zhang, Y., Bell P. R. F., & Hutchins, D. A. (2005), Phosphate uptake and growth kinetics of Trichodesmium (cyanobacteria) isolates from the North Atlantic ocean and the Great Barrier Reef, Australia, *J. Phycol.*, *41*(1), 62-73, https://doi.org/10.1111/j.1529-8817.2005.04063.x

Glibert, P. M., & Bronk, D. A. (1994), Release of dissolved organic nitrogen by marine diazotrophic cyanobacteria, Trichodesmium spp., *Appl. Environ. Microbiol.*, *60*(11), 3996-4000

Guieu, C., Bonnet, S., Petrenko, A., Menkes, C., Chavagnac, V., Desboeufs, C., Maes, C., & Moutin, T. (2018), Iron from a submarine source impacts the productive layer of the Western Tropical South Pacific (WTSP), *Sci. Rep.*, *8*, https://doi.org/10.1038/s41598-018-27407-z

Messié, M., & Chavez, F. P. (2017), Nutrient supply, surface currents, and plankton dynamics predict zooplankton hotspots in coastal upwelling systems, *Geophys. Res. Lett.*, *44*(17), 8979-8986, https://doi.org/10.1002/2017GL074322

Ruder, S. (2016), An overview of gradient descent optimization algorithms, *arXiv preprint* arXiv:1609.04747, https://arxiv.org/abs/1609.04747

Spall, J. C., & Cristion, J. A. (1994), Nonlinear adaptive control using neural networks: Estimation with a smoothed form of simultaneous perturbation gradient approximation, *Proceedings of 1994 American Control Conference-ACC'94* (Vol. 3, pp. 2560-2564), IEEE, https://doi.org/10.1109/ACC.1994.735021

Spall, J. (1998), An overview of the simultaneous perturbation method for efficient optimization, *John Hopkins APL Technical Digest*, 19(5), 482-492.

Spall, J. (2012), Stochastic Optimization. In J. Gentle, W. Härdle, and Y. Mori, (eds.) Handbook of Computational Statistics: Concepts and Methods (2nd ed.), Springer-Verlag, Heidelberg, Chapter 7, pp. 173-201.

Spungin, D., Belkin, N., Foster, R. A., Stenegren, M., Caputo, A., Pujo-Pay, M., et al. (2018), Programmed cell death in diazotrophs and the fate of organic matter in the western tropical South Pacific Ocean during the OUTPACE cruise, *Biogeosciences*, *15*(12), 3893-3908, https://doi.org/10.5194/bg-15-3893-2018

Tympakianaki, A., Koutsopoulos, H. N., & Jenelius, E. (2015), c-SPSA: Cluster-wise simultaneous perturbation stochastic approximation algorithm and its application to dynamic origin–destination matrix estimation. *Transportation Research Part C: Emerging Technologies, 55*, https://doi.org/10.1016/j.trc.2015.01.016

de Verneil, A., Rousselet, L., Doglioli, A.M., Petrenko, A. A., & Moutin, T. (2017), The fate of a southwest Pacific bloom: gauging the impact of submesoscale vs. mesoscale circulation on biological gradients in the subtropics, *Biogeosciences*, *14*(14), 3471-3486, https://doi.org/10.5194/bg-14-3471-2017

Ye, Y., Völker, C., Bracher, A., Taylor B., & Wolf-Gladrow, D. A. (2012), Environmental controls on N2 fixation by Trichodesmium in the tropical eastern North Atlantic Ocean - A model-based study, *Deep Sea Res. Part I*, *64*, 104-117, https://doi.org/10.1016/j.dsr.2012.01.004